J. Fluid Mech. (1982), *vol.* 122, *pp.* 439–465
Printed in Great Britain

Numerical study of two-dimensional peristaltic flows

By S. TAKABATAKE AND K. AYUKAWA
Department of Mechanical Engineering, Ehime University,
Matsuyama, Ehime 790, Japan

(Received 12 November 1981 and in revised form 17 March 1982)

The Navier–Stokes equations are solved numerically for two-dimensional peristaltic flows by using the finite-difference technique employing the upwind SOR method, and the velocity, pressure and stress fields for various peristaltic flows are obtained. The influences of the magnitudes of wave amplitude, wavelength and Reynolds number on the flow are investigated through numerical calculations, and the results are compared with those of the perturbation analysis. The paper is mainly concerned with elucidating the characteristics of the peristaltic flow at moderate Reynolds numbers where peristaltic pumping has a possibility of engineering application. As a result, it is found that the validity of the perturbation solutions by Jaffrin (1973) and Zien & Ostrach (1970) are restricted within a narrower range than that which they predicted, and that the reflux phenomenon in the flow does change the whole situation according to Reynolds number.

1. Introduction

When a progressive wave resulting from area contraction and expansion of an extensible tube propagates along the length of the tube, a fluid contained in the tube is mixed and transported in the direction of the wave propagation as if it were squeezed out by the moving wall. This phenomenon, called 'peristalsis', is an inherent property of any tubular organ of the human body such as the ureter, the gastro-intestinal tract, or the small blood vessels. In the last two decades the mechanism of this mixing and transporting peristaltic motion has acquired general interest in the field of hydrodynamics, and a number of studies have been undertaken with respect to peristaltic flows by applying a simple hydrodynamic model represented by sinusoidal waves. Some of them are summarized in the review by Jaffrin & Shapiro (1971). Since these studies have been developed in connection with the function of organs of the human body, many of them have been concerned with the flow within a range of small Reynolds numbers. Moreover, peristaltic pumping has been quite recently utilized for the transport of such fluids as blood, slurries, corrosive fluids, and it is desirable to prevent them from coming into contact with the mechanical parts of the pump. So it is necessary that the peristaltic flow at moderate Reynolds numbers should be analysed.

In the range of finite Reynolds number, a theoretical analysis of the peristaltic flow is extremely difficult because of the nonlinearity due to the interaction between the moving wall and the flow field. Fung & Yih (1968) first performed a study of peristaltic flow including small nonlinear effects. They treated the case of a two-dimensional channel with a small ratio of amplitude to wavelength of the peristaltic wave, and their analysis was based upon perturbations of the ratio of wave amplitude to mean

channel width. Shapiro, Jaffrin & Weinberg (1969) obtained a linear solution of peristaltic flow by considering the limiting case in which the wavelength was infinite and the fluid inertia could be neglected, and by applying Stokes' approximation to the flow. This linear solution was modified later by Jaffrin (1973) in his consideration of small nonlinear effects. He made a perturbation analysis so as to obtain the series solutions for both the case of long wavelength at zero Reynolds number and the case of small Reynolds number at infinite wavelength. The applicable range of these series solutions was studied through a comparison with experimental results (Weinberg, Eckstein & Shapiro 1971). For the limiting case of large Reynolds number with small amplitude and long wavelength, Hanin (1968) analysed the flow by applying the boundary-layer equation, and Ayukawa, Kawai & Kimura (1981) obtained experimental results as well as an approximate solution of potential flow on the basis of source distributions. In these two works, the peristaltic pumping was investigated with reference to engineering applications. On the other hand, with respect to numerical investigations, we have the analyses of Tong & Vawter (1972) and Brown & Hung (1977). The former uses the finite-element method that is available for the case of large amplitude, and the latter applies the finite-difference method by employing orthogonal curvilinear coordinates. But each of them has its disadvantage in requiring enormous and complicated calculations and/or a restriction on the geometry of the calculating region.

In this paper, the Navier–Stokes equations are solved numerically by using a finite-difference technique on the peristaltic flow induced by an infinite train of sinusoidal waves in a two-dimensional channel. Simple and appropriate oblique lattice coordinates are introduced and the governing equations are represented by the difference equations including the stream function and the vorticity as the unknowns. The upwind successive-over-relaxation method (upwind SOR method) is used to solve them. Although the theoretical analyses in the previous works are applicable only for the specific flow in which one or more simplifying assumptions are introduced on the magnitudes of wave amplitude, wavelength and Reynolds number, the present numerical method has no restriction in principle on these three quantities, so it is possible to obtain solutions in a wider range of them. Various peristaltic flows are calculated under the conditions of finite amplitudes, finite wavelengths and finite Reynolds numbers. The velocity, pressure and stress fields are obtained, and the relations between the pressure rise per wavelength and the time-mean flow that describe the primary properties of the peristaltic pumping are discussed. The trajectories of the fluid particles are also shown to exhibit the 'reflux' phenomenon. The investigation by means of numerical calculations is made on the influences of the magnitudes of wave amplitude, wavelength and Reynolds number on the flow, compared with the theoretical results obtained by the perturbation methods. In particular, the authors feel a great interest in the application of peristaltic motion to a transporting device in an engineering field; therefore the greatest part of this paper is devoted to elucidating the characteristics of the peristaltic flow in the range of moderate Reynolds number where peristaltic pumping has a possibility of engineering application.

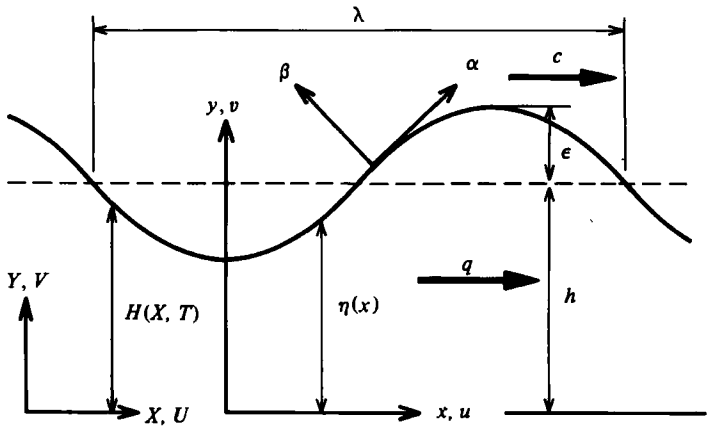

FIGURE 1. Geometry of two-dimensional peristaltic channel.

2. Governing equations and boundary conditions

We consider first the two-dimensional channel with X-axis longitudinal and Y-axis normal to it (see figure 1). The peristaltic wall of the channel is defined by the equation

$$H(X,T) = h - \epsilon \cos\frac{2\pi}{\lambda}(X - cT), \tag{1}$$

so that an infinite train of sinusoidal waves progresses along the wall in the positive X-direction with the velocity c. The plane $Y = 0$ can be interpreted either as the fixed wall of the asymmetrical channel with one wall moving or as the centre axis of the symmetrical channel with both walls moving, provided that the boundary condition on it is introduced appropriately.

In the fixed coordinates (X, Y) (the laboratory frame), the flow in the channel is unsteady because of the moving boundary. However, if observed in the moving coordinates (x, y) (the wave frame), which travel in the positive X-direction with the same speed as the waves, the developed flow can be treated as steady because the configuration of the wall appears to be stationary. The transformations between the two frames are

$$x = X - cT, \quad y = Y, \quad u = U - c, \quad v = V, \tag{2}$$

where (U, V) and (u, v) represent the velocity components in the laboratory and the wave frame respectively. In this paper, the flow will be treated as steady in the wave frame, and the flow in the laboratory frame will be derived from this steady solution by using the relationships in (2).

In the wave frame, the governing equations are the two-dimensional steady Navier–Stokes equations and the continuity equation. As is usual in the numerical analysis of the Navier–Stokes equations, the stream function ψ and the vorticity ω are introduced as follows:

$$u = \frac{\partial \psi}{\partial y}, \quad v = -\frac{\partial \psi}{\partial x}, \tag{3}$$

$$\omega = \frac{\partial v}{\partial x} - \frac{\partial u}{\partial y}. \tag{4}$$

Then the governing equations can be reduced to

$$\frac{\partial^2\psi}{\partial x^2}+\frac{\partial^2\psi}{\partial y^2}=-\omega, \tag{5}$$

$$\frac{\partial\psi}{\partial y}\frac{\partial\omega}{\partial x}-\frac{\partial\psi}{\partial x}\frac{\partial\omega}{\partial y}=\nu\left(\frac{\partial^2\omega}{\partial x^2}+\frac{\partial^2\omega}{\partial y^2}\right), \tag{6}$$

where ν denotes the kinematic viscosity of the fluid. Also, the configuration of the peristaltic wall can be represented by

$$\eta(x)=h-\epsilon\cos\frac{2\pi x}{\lambda}, \tag{7}$$

and the no-slip condition or the symmetry condition on the planes $y=0$ and $y=\eta(x)$ can be expressed as follows:

$$\left.\begin{aligned} &u=\frac{\partial\psi}{\partial y}=-c \quad \text{(fixed wall)}\\ &\frac{\partial u}{\partial y}=\frac{\partial^2\psi}{\partial y^2}=0 \quad \text{(centre axis)}\end{aligned}\right\}, \qquad v=-\frac{\partial\psi}{\partial x}=0 \quad \text{on} \quad y=0,$$

$$u=\frac{\partial\psi}{\partial y}=-c, \quad v=-\frac{\partial\psi}{\partial x}=-\frac{2\pi\epsilon}{\lambda}c\sin\frac{2\pi x}{\lambda} \quad \text{on} \quad y=\eta(x). \tag{8}$$

Moreover, since both the planes $y=0$ and $y=\eta(x)$ constitute the streamlines in the wave frame, the flow rate q in the wave frame is constant at all cross-sections of the channel. Thus the following equations can be obtained:

$$\psi=0 \quad \text{on} \quad y=0, \quad \psi=q\,(=\text{constant}) \quad \text{on} \quad y=\eta(x), \tag{9}$$

where the relation $q=\bar{Q}-ch$ holds between the flow rate q in the wave frame and the time-mean flow $\bar{Q}$ in the laboratory frame.

The dimensionless variables defined by

$$\left.\begin{aligned} &x'=\frac{x}{\lambda}, \quad y'=\frac{y}{h}, \quad u'=\frac{u}{c}, \quad v'=\frac{v}{c},\\ &\psi'=\frac{\psi}{ch}, \quad \omega'=\frac{\omega}{c/h}, \quad q'=\frac{q}{ch}, \quad \eta'=\frac{\eta}{h},\\ &p'=\frac{p}{\mu c\lambda/h^2}, \quad \sigma'=\frac{\sigma}{\mu c\lambda/h^2}, \quad \tau'=\frac{\tau}{\mu c\lambda/h^2}\end{aligned}\right\} \tag{10}$$

will be used; and the amplitude ratio ϕ, the wavenumber α, and the Reynolds number Re, are defined by

$$\phi=\frac{\epsilon}{h}, \quad \alpha=\frac{h}{\lambda}, \quad Re=\frac{ch}{\nu}\alpha. \tag{11}$$

Consequently the governing equations and the boundary conditions can be rearranged as follows:

$$\alpha^2\frac{\partial^2\psi'}{\partial x'^2}+\frac{\partial^2\psi'}{\partial y'^2}=-\omega', \tag{12}$$

$$\frac{\partial\psi'}{\partial y'}\frac{\partial\omega'}{\partial x'}-\frac{\partial\psi'}{\partial x'}\frac{\partial\omega'}{\partial y'}=\frac{1}{Re}\left(\alpha^2\frac{\partial^2\omega'}{\partial x'^2}+\frac{\partial^2\omega'}{\partial y'^2}\right), \tag{13}$$

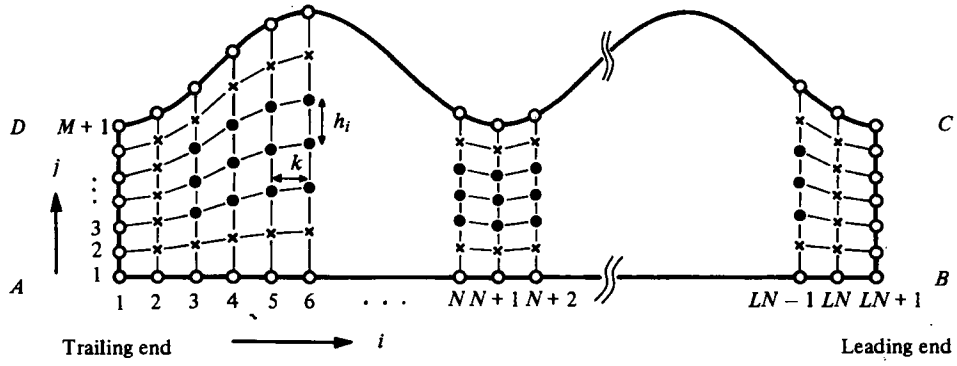

FIGURE 2. Calculating region and oblique lattice coordinates, which are employed in the numerical analysis. ○, S_{λ}; ×, P_{λ}; ●, R_{λ}.

$$\left.\begin{aligned} &\psi' = 0, \quad \frac{\partial \psi'}{\partial x'} = 0, \quad \left.\begin{aligned} &\frac{\partial \psi'}{\partial y'} = -1 \quad \text{(fixed wall)} \\ &\frac{\partial^2 \psi'}{\partial y'^2} = 0 \quad \text{(centre axis)} \end{aligned}\right\} \quad \text{on} \quad y' = 0, \\ &\psi' = q', \quad \frac{\partial \psi'}{\partial x'} = 2\pi\phi \sin 2\pi x', \quad \frac{\partial \psi'}{\partial y'} = -1 \quad \text{on} \quad y' = \eta'(x') = 1 - \phi \cos 2\pi x'. \end{aligned}\right\} \tag{14}$$

Hereinafter the primes indicating the dimensionless quantities will be omitted.

3. Numerical analysis

3.1. *Analysis of the flow field*

The flow induced by an infinite train of peristaltic waves is expected to be the same as the periodic flow that appears at the central part of the finite calculating region, where no influences of the boundary conditions at the leading and the trailing end section are found. We consider the finite region $ABCD$ with the integral number L of waves in the wave frame, as shown in figure 2. As boundary conditions, arbitrary conditions on the two end sections BC, DA and the no-slip condition or the symmetry condition on the boundaries AB, CD are considered. We thus obtain

$$\left.\begin{aligned} &\psi = 0, \quad \left.\begin{aligned} &\frac{\partial \psi}{\partial y} = -1 \quad \text{(fixed wall)} \\ &\frac{\partial^2 \psi}{\partial y^2} = 0 \quad \text{(centre axis)} \end{aligned}\right\} \quad \text{on } AB, \\ &\psi = f(y), \quad \frac{\partial \psi}{\partial x} = 0 \quad \text{on } BC, \\ &\psi = q, \quad \frac{\partial \psi}{\partial y} = -1 \quad \text{on } CD, \\ &\psi = f(y), \quad \frac{\partial \psi}{\partial x} = 0 \quad \text{on } DA, \end{aligned}\right\} \tag{15}$$

where q is the dimensionless flow rate in the wave frame and $f(y)$ is an arbitrary function, which is zero at the points A, B and equal to q at the points C, D.

Under these boundary conditions, the governing equations (12) and (13) are solved numerically in the region $ABCD$. In the analysis, simple oblique lattice coordinates are introduced, as shown in figure 2. One wave region is divided by an integral number N of meshes in the x-direction and by an integral number M in the y-direction, and the governing equations (12) and (13) and the boundary conditions (15) can be approximated by the finite-difference equations to get the numerical solutions.

A detailed description of the numerical method used here has been reported in another paper (Ayukawa & Takabatake 1982). For the convenience of readers, the derivation of the finite-difference equations is set out in the appendix and the computational procedure is presented in the following.

Among all of the lattice points included in the region $ABCD$, the points on the boundary are denoted by S_h, the interior points next to the boundary by P_h, and the other interior points by R_h. Under the conditions of the given values of ψ and its normal derivatives on S_h, we aim to obtain a numerical solution $\psi^{(l)}_{i,j}$ of (A 1) on R_h+P_h and a numerical solution $\omega^{(l)}_{i,j}$ of (A 4) on $R_h+P_h+S_h$. Computations are carried out according to the following procedure.

(i) Initially, we set

$$\psi^{(0)}_{i,j} = c_\psi \quad \text{on} \quad R_h+P_h, \quad \omega^{(0)}_{i,j} = c_\omega \quad \text{on} \quad R_h+P_h+S_h,$$

where c_ψ, c_ω are arbitrary constants.

(ii) In order to determine $\psi^{(1)}_{i,j}$ on R_h by using the SOR method, we set $\psi^{(1,0)}_{i,j} = \psi^{(0)}_{i,j}$ on R_h+P_h. We get $\psi^{(1,k)}_{i,j}$ on R_h by the use of the following recursion formula based upon (A 1):

$$\left.\begin{aligned} \overline{\psi}^{(1,k)}_{i,j} &= (1-r_\psi)\,\psi^{(1,k-1)}_{i,j} - \frac{r_\psi}{a_0}\{a_1\psi^{(1,k-1)}_{i+1,j} + a_2\psi^{(1,k-1)}_{i,j+1} + a_3\overline{\psi}^{(1,k)}_{i-1,j} \\ &\qquad + a_4\overline{\psi}^{(1,k)}_{i,j-1} + a_5\overline{\psi}^{(1,k)}_{i-1,j-1} + \omega^{(0)}_{i,j}\} \quad (0 < r_\psi < 2), \\ \psi^{(1,k)}_{i,j} &= \xi\psi^{(1,k-1)}_{i,j} + (1-\xi)\,\overline{\psi}^{(1,k)}_{i,j} \quad (0 \leqslant \xi \leqslant 1), \end{aligned}\right\} \tag{16}$$

where r_ψ denotes the relaxation factor and ξ indicates the weight factor. This inner iteration is continued until

$$|\psi^{(1,k)}_{i,j} - \psi^{(1,k+1)}_{i,j}| < \epsilon_\psi \quad \text{on} \quad R_h \tag{17}$$

is satisfied for the preset value of tolerance ϵ_ψ. After this, we define $\psi^{(1)}_{i,j} = \psi^{(1,k)}_{i,j}$ on R_h.

(iii) Substituting $\psi^{(1)}_{i,j}$ on R_h in (A 9), we can determine $\psi^{(1)}_{i,j}$ on P_h.

(iv) Next, $\omega^{(1)}_{i,j}$ on S_h can be determined from (A 7) by using $\psi^{(1)}_{i,j}$ on $R_h+P_h+S_h$ obtained in steps (i)–(iii).

(v) We proceed to determine $\omega^{(1)}_{i,j}$ on R_h+P_h by applying the SOR method again. We set first $\omega^{(1,0)}_{i,j} = \omega^{(1)}_{i,j}$ on S_h and $\omega^{(1,0)}_{i,j} = \omega^{(0)}_{i,j}$ on R_h+P_h. Then we get $\psi^{(1,K)}_{i,j}$ on R_h+P_h as in step (ii), by using the recursion formula based upon (A 4):

$$\left.\begin{aligned} \overline{\omega}^{(1,K)}_{i,j} &= (1-r_\omega)\,\omega^{(1,K-1)}_{i,j} - \frac{r_\omega}{b_0}\{b_1\omega^{(1,K-1)}_{i+1,j} + b_2\omega^{(1,K-1)}_{i,j+1} \\ &\qquad + b_3\overline{\omega}^{(1,K)}_{i-1,j} + b_4\overline{\omega}^{(1,K)}_{i,j-1} + b_5\overline{\omega}^{(1,K)}_{i-1,j-1}\} \quad (0 < r_\omega < 2), \\ \omega^{(1,K)}_{i,j} &= \delta\omega^{(1,K-1)}_{i,j} + (1-\delta)\,\overline{\omega}^{(1,K)}_{i,j} \quad (0 \leqslant \delta \leqslant 1). \end{aligned}\right\} \tag{18}$$

When

$$|\omega_{i,j}^{(1,K)} - \omega_{i,j}^{(1,K+1)}| < \epsilon_\omega \quad \text{on} \quad R_h + P_h \tag{19}$$

is satisfied for the preset value of tolerance ϵ_ω, we define $\omega_{i,j}^{(1)} = \omega_{i,j}^{(1,K)}$ on $R_h + P_h$.

(vi) Thus, after steps (ii)–(v) (the outer iteration) are repeated, we can determine the iterative solutions $\psi_{i,j}^{(1)}, \omega_{i,j}^{(1)}, \psi_{i,j}^{(2)}, \omega_{i,j}^{(2)}, \ldots$, successively. When

$$\left.\begin{aligned} |\psi_{i,j}^{(l)} - \psi_{i,j}^{(l+1)}| &< \epsilon_\psi \quad \text{on} \quad R_h + P_h, \\ |\omega_{i,j}^{(l)} - \omega_{i,j}^{(l+1)}| &< \epsilon_\omega \quad \text{on} \quad R_h + P_h + S_h \end{aligned}\right\} \tag{20}$$

are satisfied simultaneously, these numerical solutions $\psi_{i,j}^{(l)}$ and $\omega_{i,j}^{(l)}$ are taken to be the approximated ones of $\psi(x, y)$ and $\omega(x, y)$ respectively.

Although the first upwind difference used here provides iterative stability for large Reynolds number, a substantial increase in truncation error is produced because of the only first-order accuracy of this difference scheme. And also, a numerical solution in the upwind-difference scheme sometimes involves an additional error due to the effect of 'artificial viscosity' (or 'numerical viscosity'). At small Reynolds number, however, the convective terms are less important and the use of the upwind difference does not introduce serious error. Thus it is generally realized that the first-upwind-difference method has several advantages and is available to obtain usable solutions, although the artificial-viscosity effect and the truncation error must be considered when assessing the accuracy of the results (see Roache 1972).

In the present calculations, the integral numbers of meshes are chosen as $N = M = 30$ in all calculations but one. From numerical results for velocities, it is ascertained that the sensitivities of numerical solutions to the variations of N and M are always smaller than the preset criterion 10^{-4} whenever they are greater than 30. This fact indicates that the numerical results are independent of the local Reynolds number of the mesh size, and therefore that the truncation error and the artificial viscosity do not appear for this range of N and M. In the case of the calculation to be compared with the experimental results, they are exceptionally chosen as $N = M = 20$, and the accuracy in this case will be discussed later (§ 3.3).

The tolerances $\epsilon_\psi, \epsilon_\omega$, which are used in the determinations of convergences in the inner and the outer iteration process, are chosen as $\epsilon_\psi = 10^{-4}$, $\epsilon_\omega = 5 \times 10^{-4}$. The optimum values of the relaxation factors r_ψ, r_ω and the weight factors ξ, δ, which dominate the convergence and the stability of the iterations, are determined empirically to be $r_\psi = 1{\cdot}8$, $r_\omega = 0{\cdot}8$, $\xi = 0{\cdot}1$, $\delta = 0{\cdot}8$ for all calculations.

3.2. *Analysis of the pressure and the stress field*

The flow in the region of finite wavetrain obtained by the analysis in § 3.1 involves the periodic flow at the central part of the region, which is independent of the arbitrary condition assumed at the leading and the trailing end section, if the integral number L of the waves chosen is appropriately large. As mentioned earlier, this periodic flow is considered to be the same as the flow induced by an infinite train of waves. Thus the pressure field and the stress field with respect to the one-wavelength region of the periodic flow are calculated in the following manner.

From the two-dimensional steady Navier–Stokes equations, introducing the stream function ψ and the vorticity ω gives the pressure terms in dimensionless form as

$$\frac{\partial p}{\partial x} = Re\left(\frac{\partial \psi}{\partial x}\frac{\partial^2 \psi}{\partial y^2} - \frac{\partial \psi}{\partial y}\frac{\partial^2 \psi}{\partial x \partial y}\right) - \frac{\partial \omega}{\partial y}, \tag{21a}$$

$$\frac{\partial p}{\partial y} = Re\,\alpha^2\left(\frac{\partial \psi}{\partial y}\frac{\partial^2 \psi}{\partial x^2} - \frac{\partial \psi}{\partial x}\frac{\partial^2 \psi}{\partial x \partial y}\right) + \alpha^2\frac{\partial \omega}{\partial x}. \tag{21b}$$

These equations are easily approximated by the difference equations, and the values of the pressure gradients $(\partial p/\partial x)_{ij}$, $(\partial p/\partial y)_{ij}$ at each lattice point can be calculated by using ψ_{ij}, ω_{ij} obtained in § 3.1. Thus, by integrating numerically these discrete values along the lattice coordinates, the pressure values indicated by the differences from a reference pressure at the given point can be determined at all of the points in the region.

For a two-dimensional flow, the components of the stress tensor in the Cartesian coordinate system (x, y) can be described in terms of dimensionless quantities as

$$\sigma_x = 2\alpha^2\frac{\partial u}{\partial x}, \quad \sigma_y = 2\alpha\frac{\partial v}{\partial y}, \quad \tau_{xy} = \alpha\left(\frac{\partial u}{\partial y} + \alpha\frac{\partial v}{\partial x}\right). \tag{22}$$

And, considering the orthogonal curvilinear coordinate system (α, β) along the peristaltic wall (see figure 1) gives the following formulae for the components of the dimensionless stress on the wall:

$$\sigma_\alpha = \sigma_x \cos 2\theta + \tau_{xy} \sin 2\theta, \tag{23a}$$

$$\sigma_\beta = \sigma_y \cos 2\theta - \tau_{xy} \sin 2\theta, \tag{23b}$$

$$\tau_{\alpha\beta} = -\sigma_x \sin 2\theta + \tau_{xy} \cos 2\theta, \tag{23c}$$

$$\theta = \arctan\left(2\pi\phi\alpha \sin 2\pi x\right), \tag{24}$$

where θ denotes the angle of the wall slope.

Approximating (22) by the difference equations in terms of ψ_{ij} and ω_{ij}, the stress components in the (x, y)-system can be obtained at all of the points: the stress components in the (α, β)-system can then be calculated at the points on the wall.

3.3. *Comparison with experiments*

In this subsection, numerical calculations are performed for a two-dimensional asymmetrical channel with one wall fixed and the other moving, and the validity of the present analysis is confirmed through a comparison of the predicted velocity profiles with the measured ones.†

In the present analysis, the periodic flow appearing at the central part of the finite region is adopted as the solution of the flow in an infinite channel since it is not influenced by the arbitrary conditions on both the end sections. The periodicity of the flow pattern is judged from the velocity profiles on the sections at the crest and the

† The apparatus used for the experiment covered a range of large Reynolds numbers of order about 10^2–10^3. Hence, if the amplitude ratio was too small, the pressure difference between the two end sections was extremely small, being on the scale of a few mmH_2O. So the value of the pressure rise could not be measured with satisfying accuracy. For this reason, a comparison with the experiments is carried out only for velocity profiles.

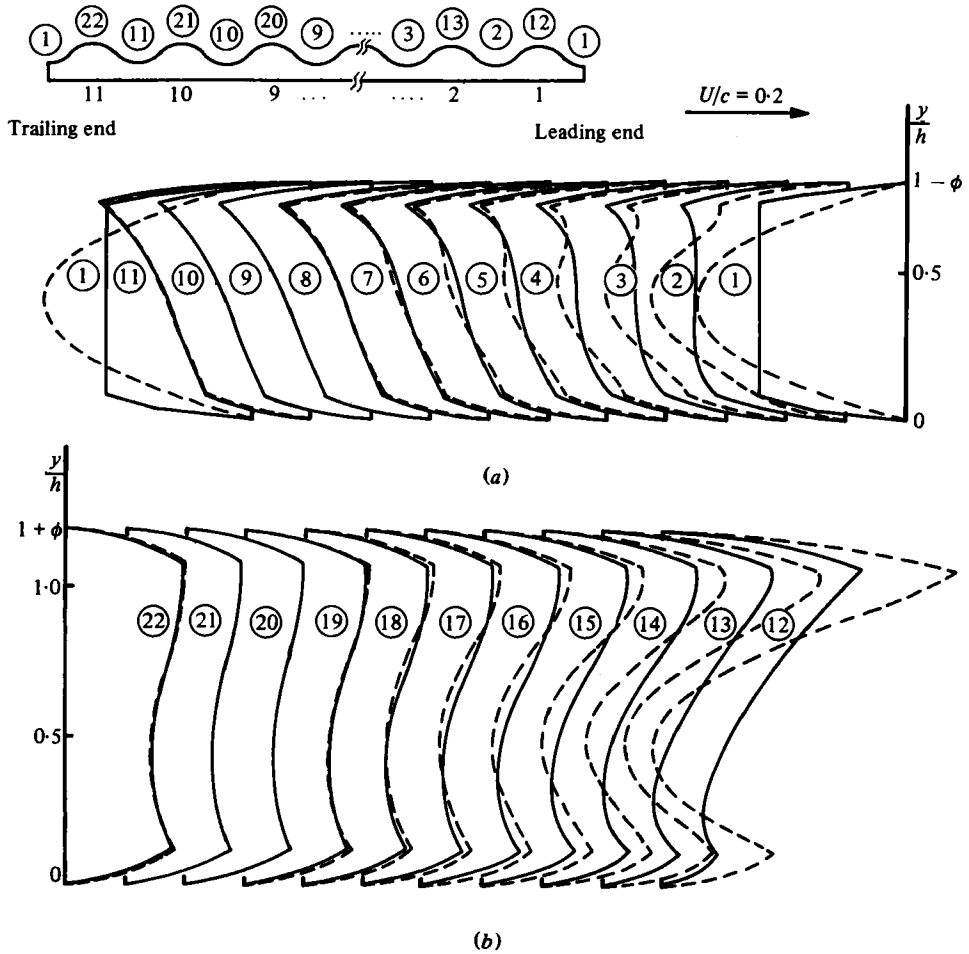

FIGURE 3. Longitudinal velocity profiles at the trough and the crest section in the finite region with eleven waves, for the asymmetrical channel; $\phi = 0{\cdot}19$, $\alpha = 0{\cdot}21$, $Re = 210$, $\overline{Q} = 0$. ——, Trapezoidal velocity profiles; – – – –, parabolic velocity profiles assumed at the leading and the trailing end section. (*a*) Trough sections. (*b*) Crest sections.

trough of the wave. Namely, when the velocity profiles on the sections at the crest and the trough are compared with the next ones, we regard the flow periodic if both absolute differences are smaller than 10^{-6}.

For the calculation in figures 3–5, because of the extremely large Reynolds number, and also because of the finite value of the wavenumber, it was required that the number L of waves had to be large. Therefore, the calculation using $N = M = 30$ failed to converge, but the stable numerical solution could be obtained after changing into $N = M = 20$. For this reason, the calculation in these figures was carried out by using $N = M = 20$. As mentioned in § 3.1, although velocities are sensitive to N and M for $(N, M) < 30$, especially in the vicinity of the wall at large Reynolds number, an error in the velocities due to the modifications of N and M from 30 to 20 was of order 10^{-2} at most, except very close to the wall.

Figure 3 shows the longitudinal velocity profiles in the laboratory frame at the trough and the crest sections in the finite region with eleven waves, which are obtained

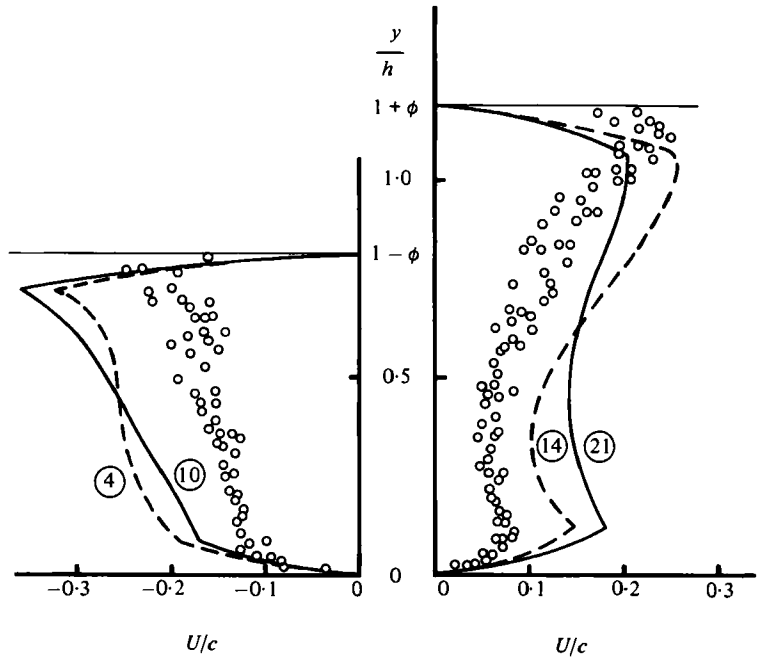

FIGURE 4. Comparison between calculated and experimental longitudinal velocity profiles for $\phi = 0{\cdot}19$, $\alpha = 0{\cdot}21$, $Re = 210$, $\bar{Q} = 0$. ——, – – – –, profile obtained by the present method in the periodic flow region and in the third wavelength region respectively; ○, experimental results of Ayukawa *et al.* (1981).

by assuming the different profiles of ψ on the end sections. In the figure, the solid curves show the results obtained by assuming ψ on both the end sections to have the trapezoidal velocity profiles, while the dashed curves are those for the parabolic velocity profiles. In both cases, the velocity profiles are influenced by ψ assumed on the leading end section, but this contribution becomes gradually weaker as they get away from it. The regular profiles independent of ψ on the end sections are observed in the central part of the region (9th and 10th wavelength region from the leading end section). The velocity profiles for the case of the trapezoidal profiles on both the end sections (shown by the solid curves in figure 3) are compared with the experimental results (Ayukawa *et al.* 1981) in figure 4. In this figure, the solid curves represent the profiles in the region at which the periodic flow pattern appears (i.e. ⑩ and ㉑ in figure 3), while the dashed curves represent those in the 3rd wavelength region from the leading end section (i.e ④ and ⑭). The dashed curves, rather than the solid curves, are in good qualitative agreement with the experimental results, and this fact is explained as follows. The measurements of the velocities were carried out in the 3rd wavelength region by using the experimental apparatus, which could impose four waves on the constant test length of the channel. Therefore the influence of the leading end section occurred in the experimental velocity profiles, and the inlet velocity profile at the leading end section was supposed to be an almost-trapezoidal form because the Reynolds number was large. It is considered that these two matters have caused the measured velocity profiles to resemble the dashed curves rather than the solid curves. Also, the quantitative difference between the predicted and the measured velocity is considered to result from the existence of leakage through the so-called

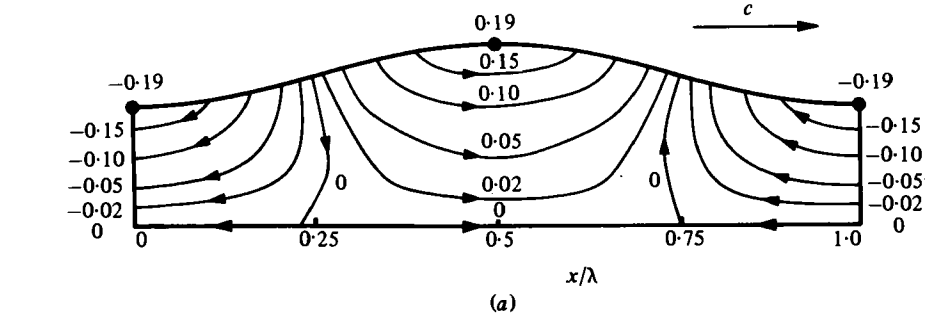

(*a*)

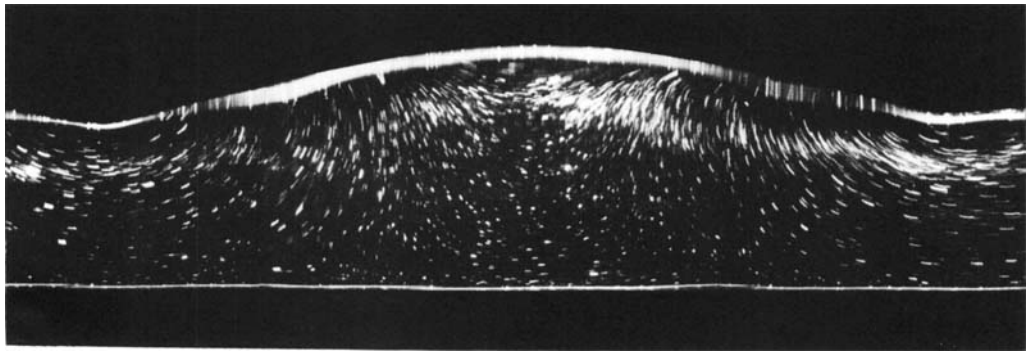

(*b*)

FIGURE 5. Laboratory-frame streamlines for $\phi = 0{\cdot}19$, $\alpha = 0{\cdot}21$, $Re = 210$, $\bar{\mathscr{Q}} = 0$. (*a*) Calculated streamlines ψ/ch. (*b*) Visualized photograph.

'inactive pumping region' of the experimental channel. Because this inactive region, on which the peristaltic waves are not imposed, acts as an inactive channel parallel to the active peristaltic channel, the fluid is forced to drift between the two channels, and the substantial operation of peristaltic pumping does fall somewhat. In taking these matters into account for the experimental results, it may be concluded that the agreement between the predicted and the measured velocity is satisfactory. A comparison between the calculated and the visualized streamlines viewed in the laboratory frame is made in figure 5.

4. Results and discussion

The problem of peristaltic flow is controlled by four dimensionless parameters: the amplitude ratio $\phi(=\epsilon/h)$ and the wavenumber $\alpha(=h/\lambda)$, which are determined by the geometry of the peristaltic wave; the Reynolds number $Re(=(ch/\nu)\alpha)$, defined from the governing equations; and the dimensionless pressure rise per wavelength $\Delta\mathscr{P}_\lambda(=h^2\Delta p_\lambda/\mu c\lambda)$ or the dimensionless time-mean flow $\bar{\mathscr{Q}}(=\bar{Q}/ch)$, which is prescribed by the boundary condition. In this section, the velocity, pressure and stress fields of the flow are calculated for various values of these four parameters in the case of a two-dimensional symmetrical channel with both walls moving. Numerical results are used for an investigation of the effects of the wave amplitude, wavelength and Reynolds number on the peristaltic flow, by comparison with the theoretical results based upon the perturbation method.

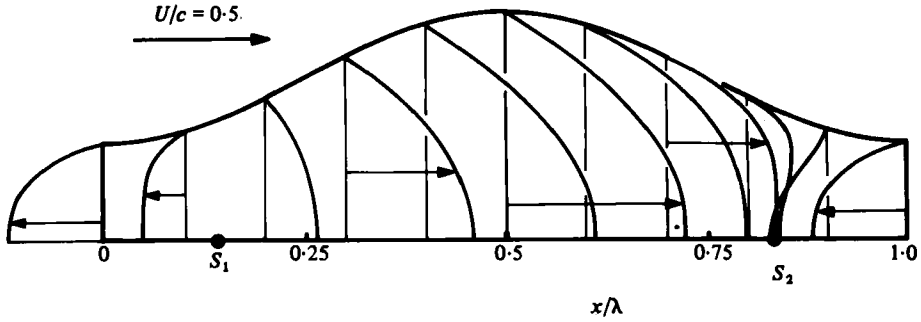

FIGURE 6. Longitudinal velocity profiles for $\phi = 0{\cdot}4$, $a = 0{\cdot}2$, $Re = 1$, $\Delta\mathscr{P}_\lambda = 0$.

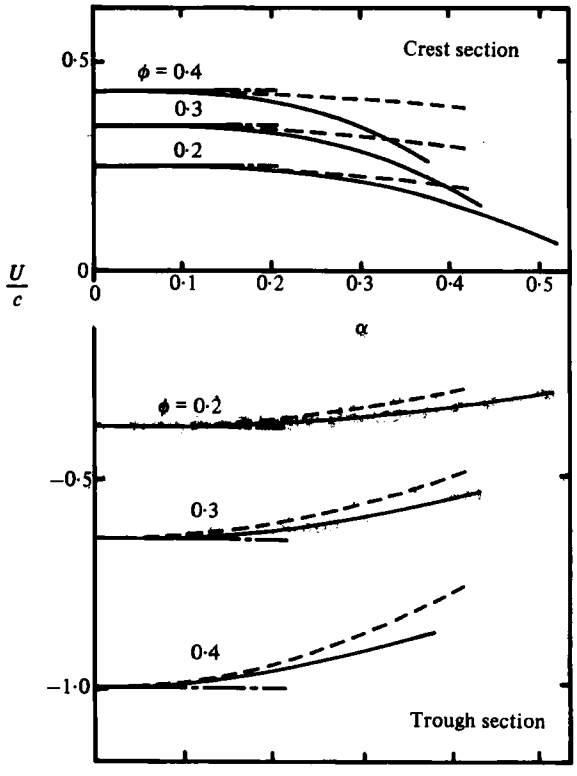

FIGURE 7. Velocities on the centre axis at the crest and the trough section for $Re = 0{\cdot}01$, $\bar{Q} = 0$. ——, present method; – · –, linear solution of Shapiro *et al.* (1969); – – – –, series solution up to order a^2 of Jaffrin (1973).

4.1. *Velocity field*

The velocity field can be calculated straightforwardly from the difference approximation to (3). As an example of numerical calculations, profiles of the longitudinal velocity U in the laboratory frame are presented in figure 6, for $\phi = 0{\cdot}4$, $a = 0{\cdot}2$, $Re = 1$, $\Delta\mathscr{P}_\lambda = 0$, when the dimensionless time-mean flow is obtained as $\bar{Q} = 0{\cdot}239$. Two stagnation points S_1 and S_2 appear along the axis near the trailing and the leading end respectively, separating the central region of a forward flow from two retrograde-flow regions. From the standpoint of peristaltic pumping, this retrograde flow at the

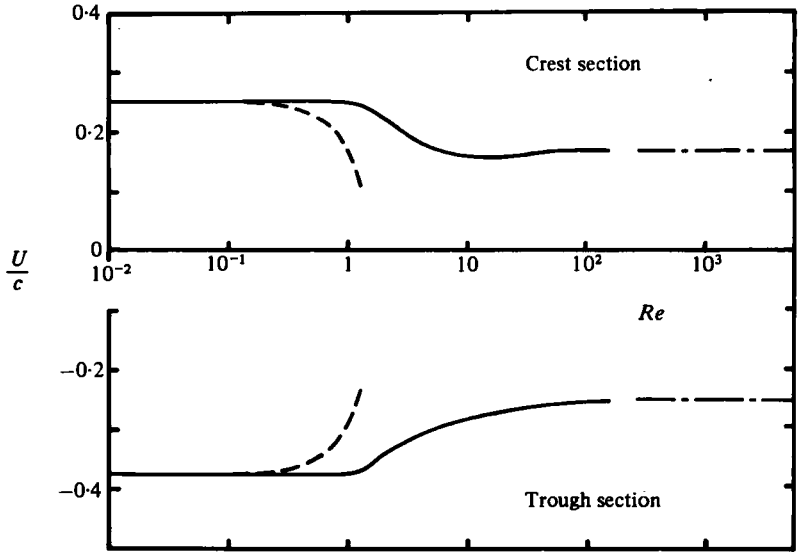

FIGURE 8. Velocities on the centre axis at the crest and the trough section for $\phi = 0{\cdot}2$, $\alpha = 0{\cdot}01$, $\bar{\mathscr{Q}} = 0$. ——, Present method; – – – –, series solution up to order Re^3 of Jaffrin (1973); – · –, solution of potential flow (Ayukawa *et al.* 1981).

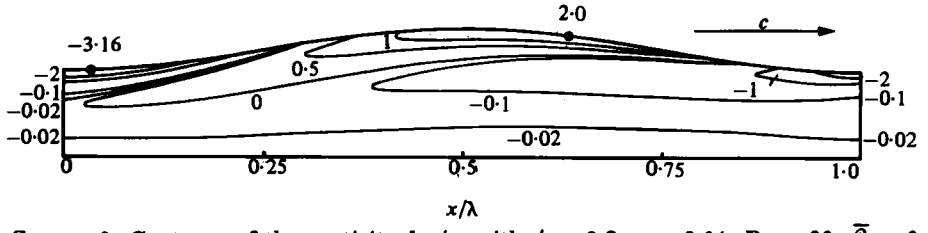

FIGURE 9. Contours of the vorticity $h\omega/c$; with $\phi = 0{\cdot}2$, $\alpha = 0{\cdot}01$, $Re = 20$, $\bar{\mathscr{Q}} = 0$.

trough region is considered to be a kind of ineffective leakage. When the time-mean flow is zero, the forward-flow region and the retrograde-flow region equally occupy half of the one-wavelength region, but the forward-flow region is here predominant because of the finite value of the time-mean flow. The profiles of U in the figure are almost parabolic at each section, supporting the solution of Shapiro *et al.* (1969) obtained for the limit $Re \to 0, \alpha \to 0$. However, the profiles at sections near the leading stagnation point S_2 are seen to be deformed slightly from the parabolic profiles, because of the effects of fluid inertia and wall slope, due respectively to the finite values of Re and α. This deformation is notable especially in the wall neighbourhood. It is therefore supposed that the mixing mechanism of peristaltic flow grows up from the neighbouring region of the wall near the leading stagnation point if Re and/or α become larger.

The effects of ϕ, α and Re upon the velocities on the axis at the crest and the trough section are shown in figures 7 and 8 in the case of zero time-mean flow, together with the linear solution of Shapiro *et al.* (1969), the second-order perturbation solution of Jaffrin (1973) and the approximate solution of potential flow (Ayukawa *et al.* 1981). In figure 7, in the range of small α at all values of ϕ the velocities on the axis are constant, and they are in coincidence with the solution of Shapiro *et al.*, while in the

range of large α their absolute values decrease with increasing α. This contribution of α to the velocities is found at smaller values of α as ϕ becomes larger. As shown in figure 8, for $Re < 1$ both velocities at the crest and the trough section are independent of Re, whereas for $Re > 1$ their absolute values decrease and approach asymptotically the solution of potential flow as Re increases. For an example of the vorticity contours at moderate Reynolds number, figure 9 represents one for $Re = 20$. The vorticity is concentrated in the region adjacent to the wall, and the vorticity in the extensive region near the axis is very small. It is ascertained from this fact that the flow at moderately large Reynolds number is almost irrotational and can be approximated well by the potential flow, except in the region adjacent to the wall.

4.2. *Trajectory of the fluid particle*

The trajectories of the fluid particles are significant objects for the investigation of the mixing mechanism of peristalsis. Shapiro *et al.* (1969) analysed the Lagrangian trajectory of a fluid particle for inertia-free flow and obtained the following conclusions. A particle period, which is the time interval until the particle occupies the same location relative to the wave as it did at the start, does not always coincide with the wave period, and fluid particles near the peristaltic wall undergo a net negative displacement called 'reflux', for small time-mean flow. Here the same arguments are developed with respect to the particle trajectory and the reflux phenomenon, extending over large Reynolds numbers.†

The trajectory of the particle can be obtained by integrating the simultaneous equations

$$\frac{dX}{dT} = U, \quad \frac{dY}{dT} = V \tag{25}$$

successively from the initial location of the particle. The integration is carried out numerically by the Runge–Kutta method.

Examples of the particle trajectories at moderate Reynolds number are shown in figure 10. In the figure, the open circles indicate the initial locations and the filled circles the locations at the end of one and two wave periods. The resultant particle periods do not coincide with the wave period, and the particle repeats the same trajectory completely for the successive particle periods. These results are identical with that obtained at small Reynolds number by Shapiro *et al.* (1969). At the end of each particle period, however, the particle near the axis (initial location is $X/\lambda = 0{\cdot}5$, $Y/h = 0{\cdot}3$) experiences a net negative longitudinal displacement, while the one near the wall ($X/\lambda = 0{\cdot}5$, $Y/h = 1{\cdot}0$) undergoes a net positive longitudinal displacement.

† There are two different definitions of 'peristaltic reflux' in the literature. One is the definition based on a Lagrangian viewpoint (Shapiro *et al.* 1969; Weinberg *et al.* 1971; Jaffrin & Shapiro 1971) and the other is that based on an Eulerian viewpoint (Fung & Yih 1968; Yin & Fung 1969, 1971; Zien & Ostrach 1970; Li 1970). Although these two definitions are made of two different phenomena, the same term 'reflux' is unfortunately used. This discrepancy induces inevitably different conclusions as to an appearance of 'reflux'. Since we are interested in the mechanism of a mixing peristaltic motion such as the retrograde motion of bacteria from the bladder to the kidneys, the appropriate quantity to investigate is considered to be the Lagrangian displacement of a particular fluid particle and not the Eulerian time-mean velocity. We therefore use 'reflux' in the Lagrangian sense for the phenomenon of a net negative displacement of a particle trajectory.

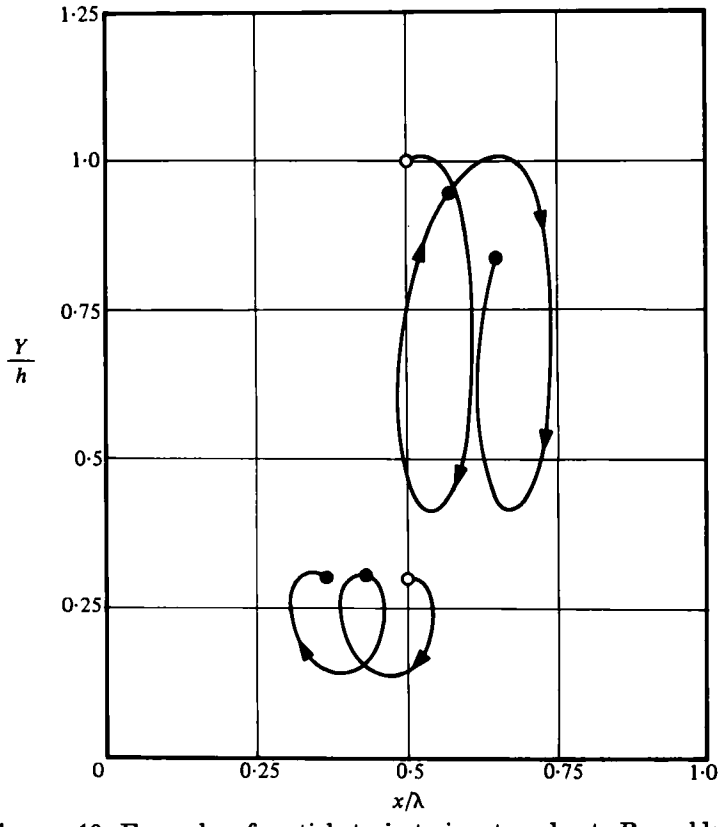

FIGURE 10. Examples of particle trajectories at moderate Reynolds number; $\phi = 0{\cdot}4$, $\alpha = 0{\cdot}01$, $Re = 10$, $\bar{Q} = 0$.

These travelling behaviours of the fluid particles are entirely opposite to that at small Reynolds number. The dependence of the longitudinal displacement of the particle at the end of one particle period upon Reynolds number and upon the lateral position at the start are illustrated in figure 11. This figure indicates that the fluid particles experience the longitudinal displacement in the opposite direction whether the Reynolds number is larger or smaller than unity. Thus it is concluded that the reflux phenomenon in the Lagrangian sense occurs near the wall for $Re < 1$, but near the axis for about $Re > 1$.

Yin & Fung (1969) mentioned that when the particle reached the same lateral location as at the start the longitudinal location relative to the wave was not generally the same as at the start and the trajectory did not immediately repeat itself. But we have obtained a result different from theirs with respect to the particle trajectory. In our investigation, the particle period of a particle undergoing a net positive displacement is always greater than the wave period, and vice versa, and the wave progresses during the difference of the particle period from the wave period so that the particle returns to the same longitudinal location relative to the wave. Therefore every particle repeats eventually the same trajectory for the successive particle periods. Because the displacements of the particles shown in figure 11 were measured on the basis of the particle period of each particle, the measured time intervals were different for individual particles at initially different lateral locations. Hence an

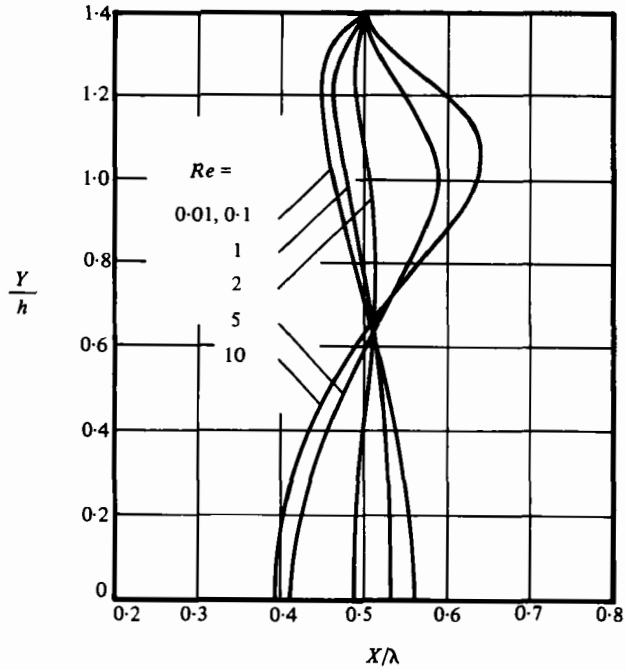

FIGURE 11. Effect of Reynolds number on the reflux phenomenon; with $\phi = 0{\cdot}4$, $\alpha = 0{\cdot}01$, $\overline{Q} = 0$.

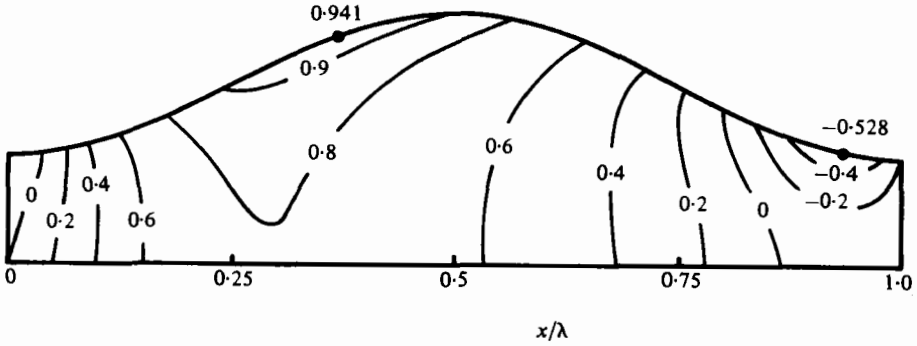

FIGURE 12. Contours of the pressure $h^2p/\mu c\lambda$ for the flow in figure 6.

integration of this displacement profile across the cross-section does not immediately give us the time-mean flow rate. If we consider the displacement on the basis of wave period, the integral value of the displacement profile in which we find some lateral displacement of the particle will be identical with the time-mean flow rate.

4.3. *Pressure field*

Figure 12 shows an example of the pressure contours, in which the pressure values relative to the reference pressure $p = 0$ at the point $x = y = 0$ are normalized in the dimensionless forms $h^2p/\mu c\lambda$. Both the maximum and the minimum pressure are seen along the peristaltic wall, and their positions are at about $x/\lambda = 0{\cdot}37$ and $0{\cdot}93$ respectively. The effects of Re on the pressure contours for the free-pumping end condition (i.e. the pressure rise per wavelength is zero) are illustrated in figure 13,

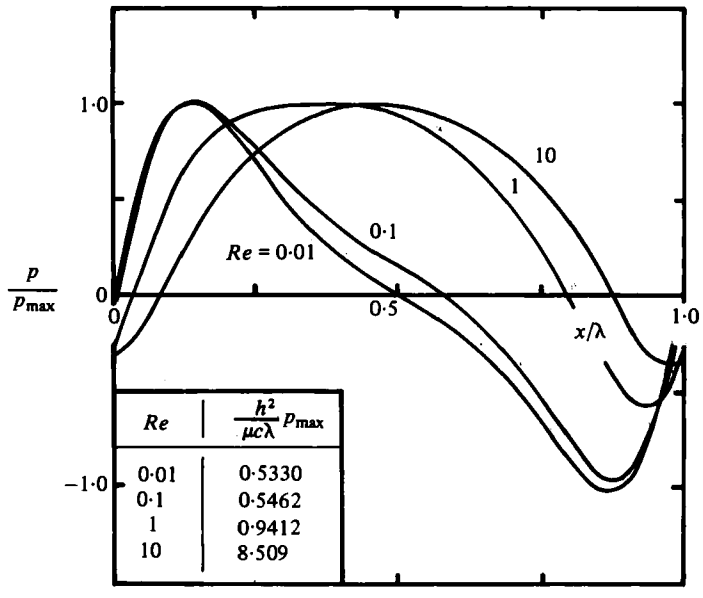

FIGURE 13. Pressure distributions along the peristaltic wall for $\phi = 0{\cdot}4$, $\alpha = 0{\cdot}2$, $\Delta\mathscr{P}_\lambda = 0$.

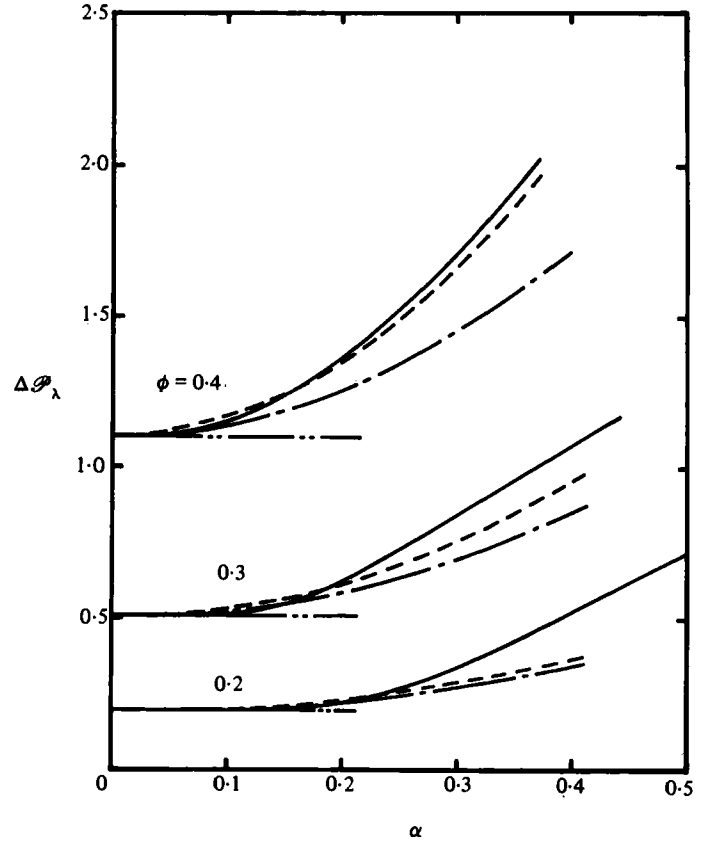

FIGURE 14. Pressure rise per wavelength for $Re = 0{\cdot}01$, $\bar{Q} = 0$. ——, Present method; – – – –, Jaffrin (1973); – · –, Zien & Ostrach (1970); – · · –, Shapiro *et al.* (1969).

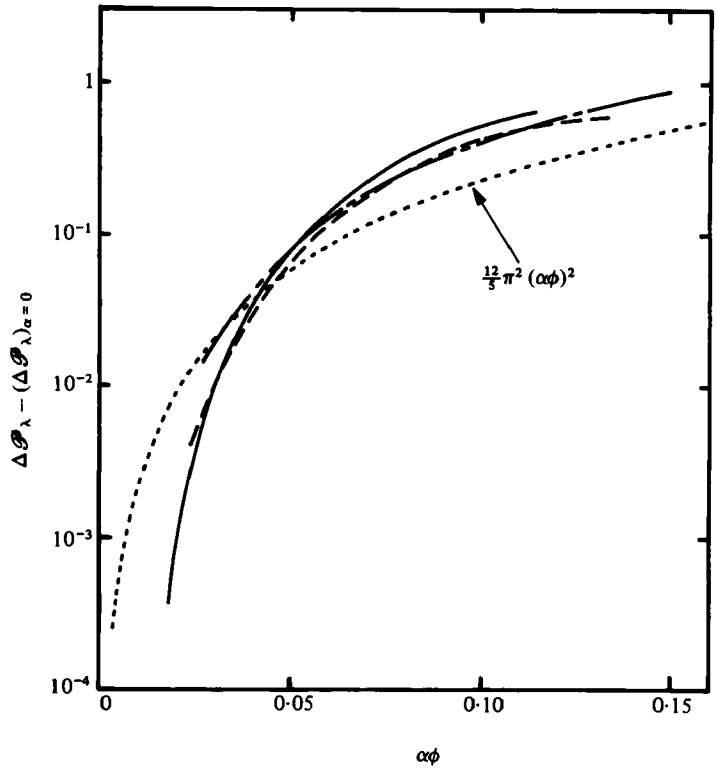

FIGURE 15. Effect of the wall slope on the pressure rise per wavelength; $Re = 0{\cdot}01$, $\bar{\mathscr{Q}} = 0$. ——, $\phi = 0{\cdot}2$; – – – –, 0·3; – · –, 0·4; · · ·, Zien & Ostrach (1970).

which shows the pressure distributions along the wall for various values of Reynolds number. When Re is extremely small, the pressure on the wall is positive at the contracting part of the channel and is negative at the dilating part. Thus the distribution along the wall is closely antisymmetric about the midsection. As Re increases, the positions of the maximum and the minimum pressure move forward (positive x-direction), and a nearly symmetrical distribution along the wall is found. In the case where the pressure distribution along the wall is nearly symmetrical about the midsection, the pressure work done by the wall is mainly cancelled between the dilating part and the contracting part. In contrast, in the case of the antisymmetrical distribution, as seen at low Reynolds numbers, the flow is given the energy equal to the pressure work done by the motion of the wall in a relatively greater degree than in the former case, and this energy is consumed in the flow as the stress work caused by the viscosity of fluid.

The dimensionless pressure rise per wavelength $\Delta\mathscr{P}_\lambda$, at zero time-mean flow, is plotted against α for various values of ϕ in figure 14. Both solutions of Jaffrin (1973) and Zien & Ostrach (1970) in the figure are the series solutions up to order α^2 based upon the perturbation analysis. In the present results, $\Delta\mathscr{P}_\lambda$ is caused to increase by the effect of the wall slope as α increases, and this contribution appears at smaller α as ϕ increases. A similar tendency has been encountered in the results of velocities on the axis, as mentioned in § 4.1; therefore it is supposed that the product of α and ϕ (i.e. ϵ/λ) is the significant geometric factor that controls the flow field in the peri-

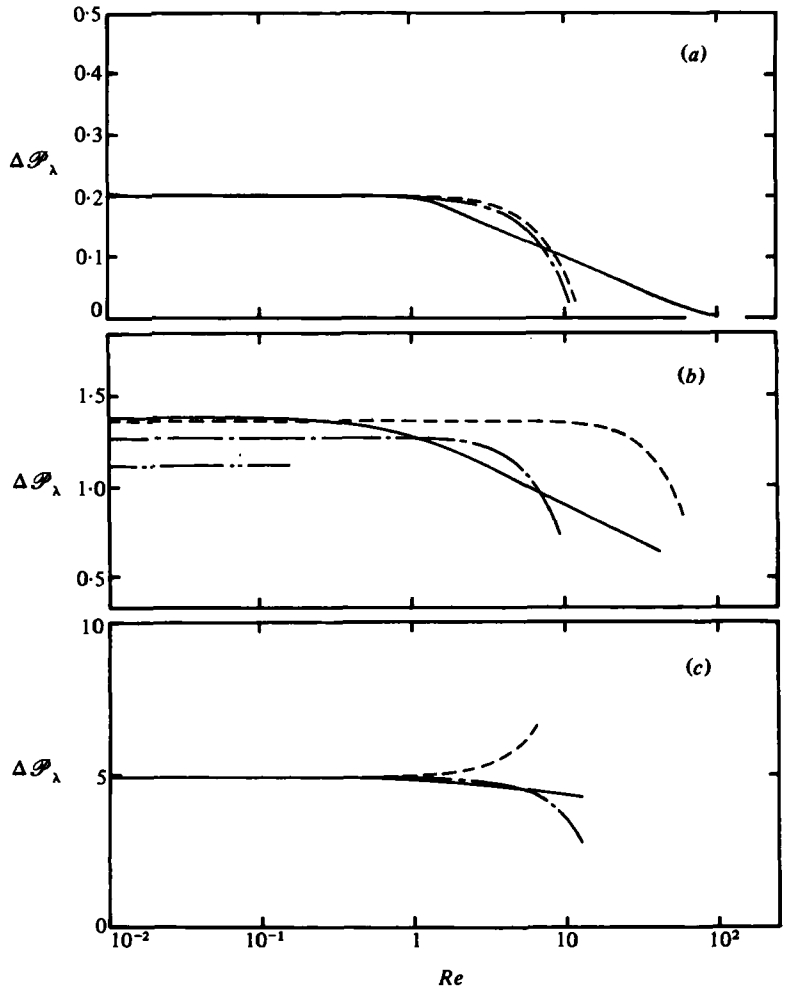

FIGURE 16. Pressure rise per wavelength for $\overline{Q} = 0$, compared with other theoretical results. ——, Present method; – – – –, Jaffrin (1973); – · –, Zien & Ostrach (1970); – · · –, Shapiro *et al.* (1969). (*a*) $\phi = 0{\cdot}2$, $\alpha = 0{\cdot}01$; (*b*) 0·4, 0·2; (*c*) 0·6, 0·01.

staltic channel. Thus we try to rearrange these results as the plots against the parameter $\alpha\phi$ in figure 15, where the ordinate $\Delta\mathscr{P}_\lambda - (\Delta\mathscr{P}_\lambda)_{\alpha=0}$ indicates directly the contribution of the wall slope effect to the pressure rise per wavelength. The curves of the present results are gathered up very well, and may be expressed approximately by one curve, in spite of different values of ϕ. In the analysis of Zien & Ostrach, the contribution of α to the pressure rise per wavelength is expressed by the second-order term as $\frac{1}{5}\pi^2(\alpha\phi)^2$, which is presented as a function of $\alpha\phi$, though some difference is found between this and the present results. Jaffrin also obtained the second-order term in the form

$$\tfrac{1}{5}\pi^2\alpha^2\left[4+\frac{7\phi^2-4}{(1-\phi^2)^{\frac{5}{2}}}\right].$$

Although this solution can be reduced to a function of $\alpha\phi$ corresponding to the solution of Zien & Ostrach for $\phi \ll 1$, it is impossible to do this in the range of moderately large

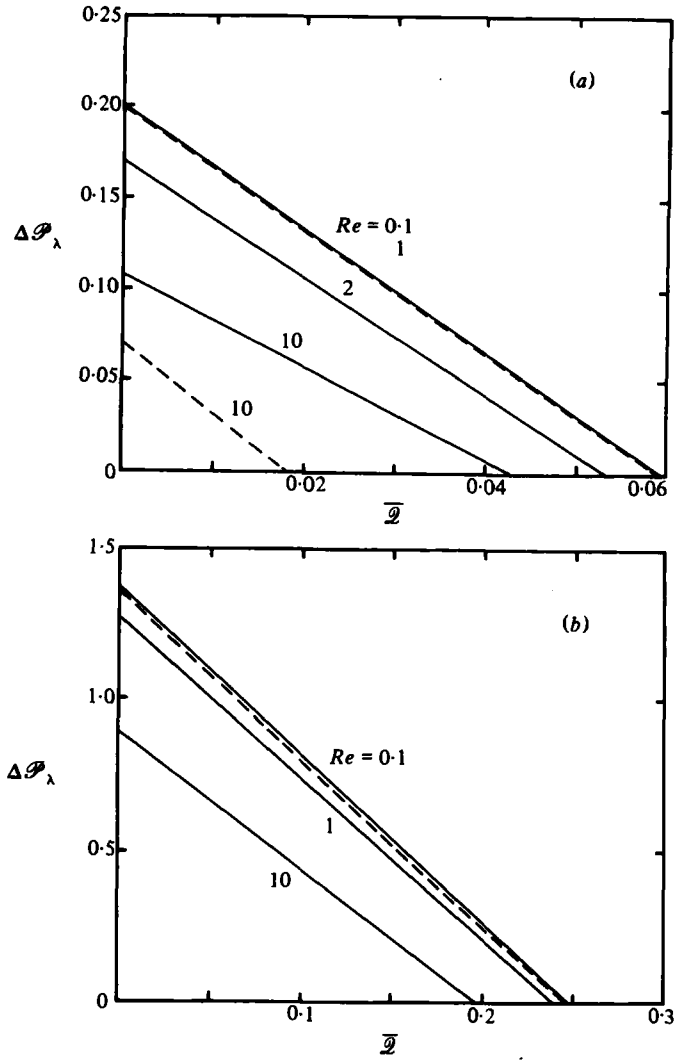

FIGURE 17. Pressure–flow characteristics for various Reynolds numbers. ——, Present method; – – – –, Jaffrin (1973). (*a*) $\phi = 0{\cdot}2$, $\alpha = 0{\cdot}01$; (*b*) 0·4, 0·2.

value of ϕ. Figure 16 shows the effects of fluid inertia on pressure rise at zero time-mean flow for three cases of different values of α and ϕ, as compared with the analytical results. In all cases $\Delta\mathscr{P}_\lambda$ is constant and independent of Re for about $Re < 1$, and decreases monotonically with increasing Re for $Re > 1$. In figures 16(*a*, *c*) constant values of $\Delta\mathscr{P}_\lambda$ for $Re \to 0$ are coincident with the other results, whereas in figure 16(*b*) they disagree with each other owing to the difference in the estimations of the effect of α on $\Delta\mathscr{P}_\lambda$. In particular, Jaffrin mentions that the inertia effect makes the pressure rise increase in case of large amplitude ratio of $\phi > 0{\cdot}4$, in contrast to the tendency for $\phi \leqslant 0{\cdot}4$, but the present result for $\phi = 0{\cdot}6$ shows that the inertia effect makes the pressure rise decrease with the same tendency for $\phi \leqslant 0{\cdot}4$. This is in contrast to the prediction of Jaffrin's analysis.

A pumping performance of the peristalsis is suitable for the transport of a particular fluid which it is necessary to prevent from coming into contact with the mechani-

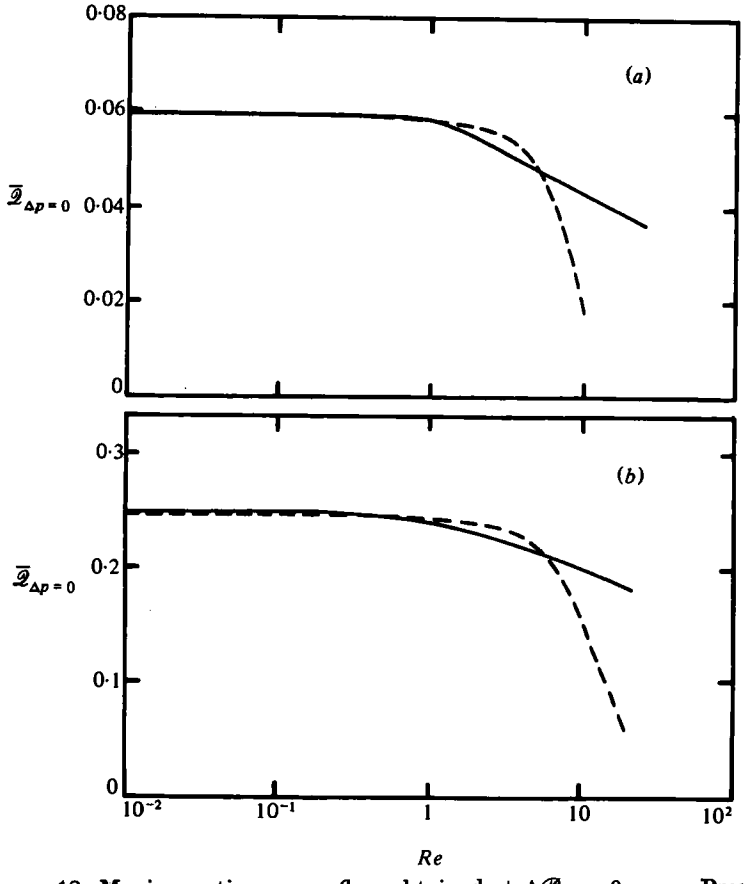

FIGURE 18. Maximum time-mean flow obtained at $\Delta\mathscr{P}_\lambda = 0$. ——, Present method; – – – –, Jaffrin (1973). (*a*) $\phi = 0{\cdot}2$, $\alpha = 0{\cdot}01$; (*b*) 0·4, 0·2.

cal parts. In order to investigate the possibilities of peristaltic pumping for engineering application, we examine the relation between the pressure rise per wavelength and the time-mean flow (i.e. the pressure–flow characteristic), which is equivalent to the relation between the total head and the flow rate in the pump. For the two cases of different amplitude ratio, the pressure–flow characteristics for various Reynolds numbers are presented in figure 17. The relation between the pressure rise per wavelength $\Delta\mathscr{P}_\lambda$ and the time-mean flow $\bar{\mathscr{Q}}$, represented in dimensionless forms, can be expressed by a straight line with negative slope for any value of Re, and the slope of the line becomes slightly gentler as Re increases. In the range of large Re, a considerable disagreement is found between the present result and Jaffrin's because of the difference in the estimations of the effect of Re upon $\Delta\mathscr{P}_\lambda$ as shown in figure 16, but for extremely small values of Re they are in good agreement. Figure 18 shows the time-mean flow for zero pressure rise, which is interpreted as the maximum time-mean flow transported by the peristaltic pumping. In considering the peristaltic device as a pump, it is in this quantity that there is a practical interest.

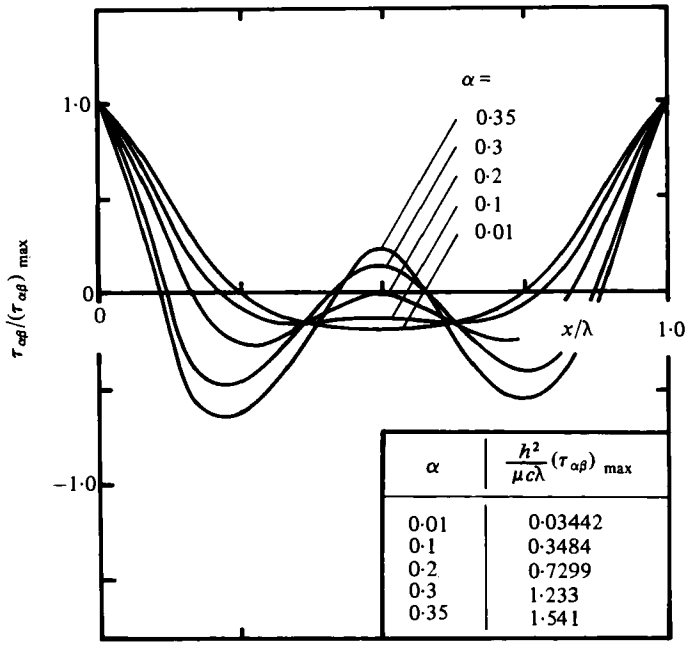

α	$\frac{h^2}{\mu c\lambda}(\tau_{\alpha\beta})_{max}$
0·01	0·03442
0·1	0·3484
0·2	0·7299
0·3	1·233
0·35	1·541

FIGURE 19. Shearing stress distributions along the peristaltic wall for $\phi = 0{\cdot}4$, $Re = 0{\cdot}01$, $\bar{\mathcal{Q}} = 0$.

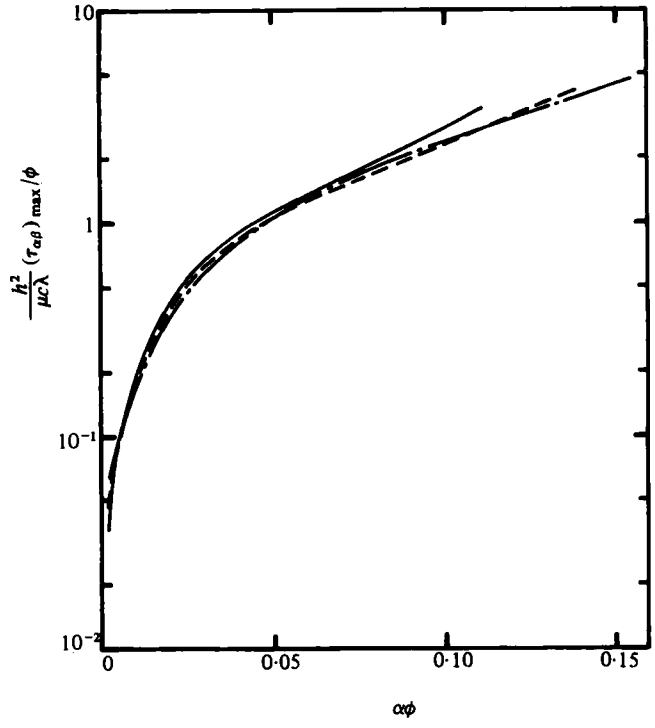

FIGURE 20. Maximum shearing stress on the peristaltic wall for $Re = 0{\cdot}01$, $\bar{\mathcal{Q}} = 0$. ——, $\phi = 0{\cdot}2$; – – – –, 0·3; – · –, 0·4.

4.4. *Shearing stress along the wall*

The investigation of shearing stress in a flow field is a significant problem, because strong shearing stress may cause damage to blood elements, for example, when blood is employed as the working fluid; the same reason also holds in other fluids.

The distributions of shearing stress along the wall for zero time-mean flow are illustrated in figure 19 for various values of α. In this case, since Re is very small, the distributions are almost symmetric about the midsection. Although for small α shearing stresses vary slightly along the wall, for large α the steep variations are found in the distributions and the maximum shearing stresses on the wall become remarkably large. As in § 4.3, by rearranging these maximum shearing stresses as functions of $\alpha\phi$, they may be represented well by one curve, as shown in figure 20, in spite of different values of ϕ.

5. Concluding remarks

On investigating the effects of the geometrical shape of the peristaltic wave upon the flow field, the numerical results for the pressure rise and for the shearing stress can be correlated in terms of $\alpha\phi$, as shown in figures 15 and 20. This fact indicates that the parameter $\alpha\phi$ is a significant factor in controlling the peristaltic flow, and suggests that in the perturbation analysis the expansion with $\alpha\phi$ is more effective than that with α or with ϕ alone, as has been usual in previous work (e.g. Fung & Yih 1968; Zien & Ostrach 1970; Jaffrin 1973).

From the results of figure 16, it has been elucidated that the magnitude of Re at which the fluid-inertia effect appears in the whole region of the flow field is about unity, and it becomes somewhat smaller than unity in the case of a wave with a steep slope (i.e. with large $\alpha\phi$). The perturbation solutions of Jaffrin (1973) and Zien & Ostrach (1970) are found to be valid in a narrower range of Re than that which they predicted, when compared with our analysis. It is supposed in our research that the applicable range of the perturbation method is nearly the same as that in the inertia-free analysis of Shapiro *et al.* (1969) for practical use.

The reflux phenomenon is found near the centre axis at large Reynolds number, although it occurs near the wall for small Reynolds number, as pointed out by Shapiro *et al.* The motion of a fluid particle depends on the distribution of Eulerian velocities in the channel. While their profiles are locally of Poiseuille type in an inertia-free case, they are rather suggestive of plug flows at large Reynolds number. This difference in the velocity fields causes the different behaviour of a fluid particle according to whether the Reynolds number is small or large.

The authors wish to express their gratitude to Professor K. Morita of Ehime University, Dr Y. Tsujimoto and Professor K. Imaichi of Osaka University, and the referees, for their kind and useful advice in revising the manuscript.

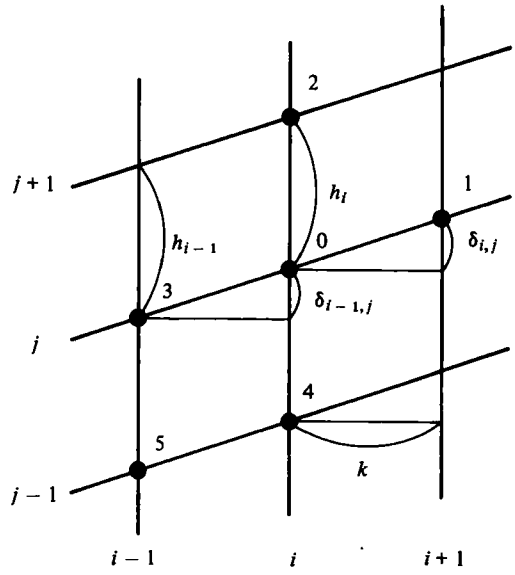

FIGURE 21. Lattice points on the interior region.

Appendix. A finite-difference method

We consider six lattice points on the interior region as shown in figure 21. The differential equation (12) can be transformed into the following finite-difference equation with a second-order accuracy when centred differences are used:

$$a_0\psi_{i,j}+a_1\psi_{i+1,j}+a_2\psi_{i,j+1}+a_3\psi_{i-1,j}+a_4\psi_{i,j-1}+a_5\psi_{i-1,j-1}+\omega_{i,j}=0 \quad (i=3,\ldots,N-1;\ j=3,\ldots,M-1), \tag{A 1}$$

where

$$\left.\begin{aligned} a_0 &= -\frac{2}{h_i^2}-\frac{\alpha^2}{k^2}(2+D_{i,j}), \quad a_1=\frac{\alpha^2}{k^2}, \quad a_2=\frac{1}{h_i^2}+\frac{\alpha^2}{2k^2}(D_{i,j}-2K_{i,j}),\\ a_3 &= \frac{\alpha^2}{k^2}(1+M_{i,j}), \quad a_4=\frac{1}{h_i^2}+\frac{\alpha^2}{2k^2}(D_{i,j}+2K_{i,j}), \quad a_5=-\frac{\alpha^2}{k^2}M_{i,j}, \end{aligned}\right\} \tag{A 2}$$

$$\left.\begin{aligned} D_{i,j} &= \left(\frac{\delta_{i,j}+\delta_{i-1,j}}{h_i}\right)^2+\frac{h_{i-1}}{h_i}\left(\frac{\delta_{i,j}+\delta_{i-1,j}}{h_i}\right)-2\left(\frac{\delta_{i,j}}{h_i}\right)^2, \quad K_{i,j}=\frac{\delta_{i,j}}{h_i},\\ M_{i,j} &= \frac{\delta_{i,j}+\delta_{i-1,j}}{h_{i-1}}, \quad S_{i,j}=\frac{\delta_{i,j}+\delta_{i-1,j}}{h_i}, \quad T_{i,j}=\frac{\delta_{i,j}-\delta_{i-1,j}}{h_i}. \end{aligned}\right\} \tag{A 3}$$

We shall now try to derive the finite-difference equation approximating to (13). In this derivation, approximations to the convective terms of (13) are done by the first upwind-difference technique (see e.g. Greenspan 1968), which is superior in stability and convergence for nonlinear terms, while the diffusive terms are approximated by using centred-difference methods. The resulting finite-difference expression for (13) is obtained as follows on the interior points:

$$b_0\omega_{i,j}+b_1\omega_{i+1,j}+b_2\omega_{i,j+1}+b_3\omega_{i-1,j}+b_4\omega_{i,j-1}+b_5\omega_{i-1,j-1}=0 \quad (i=2,\ldots,N;\ j=2,\ldots,M), \tag{A 4}$$

where

$$\left.\begin{aligned} b_0 &= a_0+\frac{Re}{2kh_i}(-|\beta|-|\gamma|+\operatorname{sgn}(\beta)\operatorname{sgn}(\gamma)\tfrac{1}{2}\gamma T_{i,j}), \quad b_1 = a_1+\frac{Re}{2kh_i}\gamma\{H(\gamma)-1\},\\ b_2 &= a_2+\frac{Re}{2kh_i}(|\beta|-\operatorname{sgn}(\beta)\operatorname{sgn}(\gamma)\tfrac{1}{2}\gamma T_{i,j})H(\beta), \quad b_3 = a_3+\frac{Re}{2kh_i}\gamma H(\gamma),\\ b_4 &= a_4+\frac{Re}{2kh_i}(-|\beta|+\operatorname{sgn}(\beta)\operatorname{sgn}(\gamma)\tfrac{1}{2}\gamma T_{i,j})\{H(\beta)-1\}, \quad b_5 = a_5, \end{aligned}\right\} \tag{A 5}$$

$$\left.\begin{aligned} &\beta = \psi_{i+1,j}-\psi_{i-1,j}, \quad \gamma = \psi_{i,j+1}-\psi_{i,j-1},\\ &\operatorname{sgn}(x) = \begin{cases} 1 & (x>0)\\ 0 & (x=0)\\ -1 & (x<0)\end{cases}, \quad H(x) = \begin{cases}1 & (x\geqslant 0)\\ 0 & (x<0)\end{cases}. \end{aligned}\right\} \tag{A 6}$$

Next, we consider four or five points on and near the boundary (figure 22) to obtain the difference approximation to ω at the boundary. The following equations are derived by expanding ψ into a Taylor series around the point numbered 0 and by using (15):

$$\left.\begin{aligned} &\omega_{i,j} = -\frac{2}{h_i^2}\psi_{i,j+1}-\frac{2}{h_i} \quad \text{(fixed wall)} \quad \text{or} \quad 0 \quad \text{(centre axis)} \\ &\qquad\qquad (i=1,\ldots,N+1;\ j=1),\\ &\omega_{i,j} = d_{0,j}\psi_{i,j}+d_{1,j}\psi_{i-1,j}+d_{2,j}\psi_{i-2,j}+d_{3,j}\psi_{i,j+1}+d_{4,j}\psi_{i,j-1}\\ &\qquad\qquad (i=N+1;\ j=2,\ldots,M),\\ &\omega_{i,j} = e_{0,i}\psi_{i,j-1}+e_{1,i}\psi_{i-1,j-1}+e_{2,i}q+e_{3,i} \quad (i=2,\ldots,N;\ j=M+1),\\ &\omega_{i,j} = d_{0,j}\psi_{i,j}+d_{1,j}\psi_{i+1,j}+d_{2,j}\psi_{i+2,j}+d_{3,j}\psi_{i,j+1}+d_{4,j}\psi_{i,j-1}\\ &\qquad\qquad (i=1;\ j=2,\ldots,M),\\ &\omega_{i,j} = f_0\psi_{i,j-1}+f_1\psi_{i-1,j-1}+f_2q+f_3 \quad (i=N+1;\ j=M+1),\\ &\omega_{i,j} = f_0\psi_{i,j-1}+f_1\psi_{i+1,j-1}+f_2q+f_3 \quad (i=1;\ j=M+1), \end{aligned}\right\} \tag{A 7}$$

where

$$\left.\begin{aligned} &d_{0,j} = \frac{2}{h_1^2}+\frac{\alpha^2}{k^2}\left(\frac{S_{2,j}+K_{2,j}}{T_{2,j}}+K_{1,j}M_{2,j}\right), \quad d_{1,j} = -\frac{2\alpha^2}{k^2}\frac{S_{2,j}}{T_{2,j}}, \quad d_{2,j} = \frac{\alpha^2}{k^2}\frac{h_1}{h_2}\frac{K_{1,j}}{T_{2,j}},\\ &d_{3,j} = -\frac{1}{h_1^2}-\frac{\alpha^2}{2k^2}K_{1,j}M_{2,j}\left(1-\frac{h_1}{h_2}\frac{1}{T_{2,j}}\right), \quad d_{4,j} = -\frac{1}{h_1^2}-\frac{\alpha^2}{2k^2}K_{1,j}M_{2,j}\left(1+\frac{h_1}{h_2}\frac{1}{T_{2,j}}\right),\\ &e_{0,i} = -\frac{2}{h_i^2}-\frac{\alpha^2}{k^2}D_{i,M+1}, \quad e_{1,i} = \frac{\alpha^2}{k^2}M_{i,M+1},\\ &e_{2,i} = \frac{1}{h_i^2}+\frac{\alpha^2}{k^2}(D_{i,M+1}-M_{i,M+1}), \quad e_{3,i} = \frac{2}{h_i}-\frac{\alpha^2}{k^2}(2\delta_{i,M+1}-h_iD_{i,M+1}),\\ &f_0 = -\frac{2}{h_1^2}-\frac{2\alpha^2}{k^2}K_{1,M+1}\left(K_{1,M+1}-\frac{h_2}{h_1}\right), \quad f_1 = -\frac{2\alpha^2}{k^2}\frac{h_1}{h_2}K_{1,M+1},\\ &f_2 = \frac{2}{h_1^2}+\frac{2\alpha^2}{k^2}K_{1,M+1}\left(K_{1,M+1}-\frac{h_2}{h_1}+\frac{h_1}{h_2}\right), \quad f_3 = \frac{2}{h_1}+\frac{2\alpha^2}{k^2}K_{1,M+1}(h_1K_{1,M+1}-h_2). \end{aligned}\right\} \tag{A 8}$$

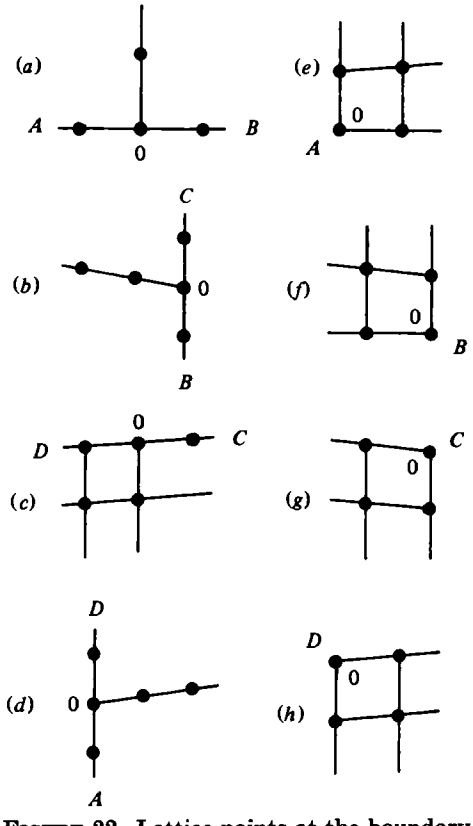

FIGURE 22. Lattice points at the boundary.

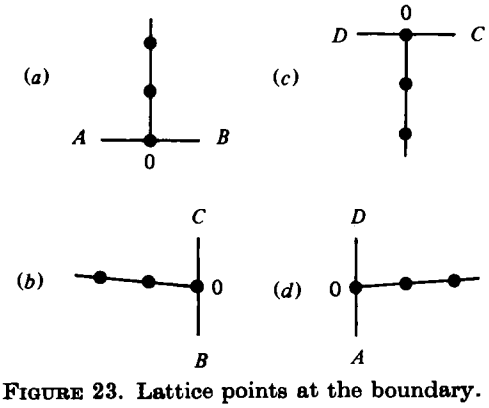

FIGURE 23. Lattice points at the boundary.

Finally, three points are considered on and near the boundary (figure 23). The following expressions for ψ at the interior points next the boundary are immediately obtained from (15):

$$\left.\begin{aligned}
&\psi_{i,j} = \tfrac{1}{4}(\psi_{i,j+1} - 2h_i) \quad \text{(fixed wall)} \quad \text{or} \quad \tfrac{1}{2}\psi_{i,j+1} \quad \text{(centre axis)} \\
&\qquad\qquad\qquad\qquad\qquad\qquad\qquad\qquad\qquad\qquad (i = 2, \ldots, N;\ j = 2), \\
&\psi_{i,j} = \frac{\delta_{i-1,j}\psi_{i+1,j} + \delta_{i,j}\psi_{i-1,j}}{\delta_{i,j} + \delta_{i-1,j}} \quad (i = N;\ j = 2, \ldots, M), \\
&\psi_{i,j} = \tfrac{1}{4}(\psi_{i,j-1} + 3q + 2h_i) \quad (i = 2, \ldots, N;\ j = M), \\
&\psi_{i,j} = \frac{\delta_{i,j}\psi_{i-1,j} + \delta_{i-1,j}\psi_{i+1,j}}{\delta_{i-1,j} + \delta_{i,j}} \quad (i = 2;\ j = 2, \ldots, M).
\end{aligned}\right\} \tag{A 9}$$

REFERENCES

AYUKAWA, K., KAWAI, T. & KIMURA, M. 1981 Streamlines and path lines in peristaltic flows at high Reynolds numbers. *Bull. Japan Soc. Mech. Engrs* **24**, 948–955.

AYUKAWA, K. & TAKABATAKE, S. 1982 Numerical analysis of two-dimensional peristaltic flows (1st report; Flow pattern). *Bull. Japan Soc. Mech. Engrs* **25** (to be published).

BROWN, T. D. & HUNG, T.-K. 1977 Computational and experimental investigations of two-dimensional nonlinear peristaltic flows. *J. Fluid Mech.* **83**, 249–272.

FUNG, Y. C. & YIH, C. S. 1968 Peristaltic transport. *Trans. A.S.M.E.*, E, *J. Appl. Mech.* **35**, 669–675.

GREENSPAN, D. 1968 *Lectures on the Numerical Solution of Linear, Singular, and Nonlinear Differential Equations*, pp. 122–147. Prentice-Hall.

HANIN, M. 1968 The flow through a channel due to transversely oscillating walls. *Israel J. Tech.* **6**, 67–71.

JAFFRIN, M. Y. 1973 Inertia and streamline curvature effects on peristaltic pumping. *Int. J. Engng Sci.* **11**, 681–699.

JAFFRIN, M. Y. & SHAPIRO, A. H. 1971 Peristaltic pumping. *A. Rev. Fluid Mech.* **3**, 13–36.

LI, C. H. 1970 Peristaltic transport in circular cylindrical tubes. *J. Biomech.* **3**, 513–523.

ROACHE, P. J. 1972 *Computational Fluid Dynamics*, §3-A-8. Hermosa.

SHAPIRO, A. H., JAFFRIN, M. Y. & WEINBERG, S. L. 1969 Peristaltic pumping with long wavelengths at low Reynolds number. *J. Fluid Mech.* **37**, 799–825.

TONG, P. & VAWTER, D. 1972 An analysis of peristaltic pumping. *Trans. A.S.M.E.* E, *J. Appl. Mech.* **39**, 857–862.

WEINBERG, S. L., ECKSTEIN, E. C. & SHAPIRO, A. H. 1971 An experimental study of peristaltic pumping. *J. Fluid Mech.* **49**, 461–479.

YIN, F. & FUNG, Y. C. 1969 Peristaltic waves in circular cylindrical tubes. *Trans. A.S.M.E.* E, *J. Appl. Mech.* **36**, 579–587.

YIN, F. & FUNG, Y. C. 1971 Comparison of theory and experiment in peristaltic transport. *J. Fluid Mech.* **47**, 93–112.

ZIEN, T. F. & OSTRACH, S. 1970 A long wave approximation to peristaltic motion. *J. Biomech.* **3**, 63–75.